Journal of Biological Engineering

RESEARCH Open Access

Chitosan biomineralized with ions-doped nano-hydroxyapatite tunes osteoblasts metabolism and DNA damage

Franco Furlani[1,2,3*], Matilde Clarissa Malfatti[1,4], Alfredo Rondinella[2], Elisabetta Campodoni[3], Monica Sandri[3], Lorenzo Fedrizzi[2] and Gianluca Tell[1]

Abstract

Hydroxyapatite (HA) is a bioceramic material widely used as a bone biomimetic substitute and can be synthesized by biomineralization, according to which HA nanoparticles are formed on a polymer template. Nevertheless, little is known about the effect of ion doping and biomineralization on cell metabolism, oxidative stress, and DNA damage. In the present contribution, we report on synthesizing and characterizing biomineralized chitosan as a polymer template with HA nanoparticles doped with magnesium (MgHA) and iron ions (FeHA). The physical-chemical and morphological characterization confirmed the successful synthesis of low crystalline ions-doped HA nanoparticles on the chitosan template, whereas the biochemical activity of the resulting nanoparticles towards human osteoblasts-like cells (MG63 and HOBIT) was investigated considering their effect on cell metabolism, proliferation, colony formation, redox status, and DNA damage extent. Data obtained suggest that particles enhance cell metabolism but partially limit cell proliferation. The redox status of cells was measured suggesting a slight increase in Reactive Oxygen Species production with chitosan biomineralized with iron-doped HA, whereas no effect with magnesium-doped HA and no effect of all formulations on the oxidation level of Peroxiredoxin. On the other hand, DNA damage was investigated by COMET assay, and expression and foci γH2AX. These latter tests indicated that HA-based nanoparticles promote DNA damage which is enhanced by chitosan thus suggesting that chitosan favors the nanoparticles' internalization by cells and modulates their biological activity. The potential DNA damage should be considered – and potentially exploited for instance in anticancer treatment – when HA-based particles are used to devise biomaterials.

Keywords DNA damage, Oxidative stress, Hydroxyapatite, Nanoparticles, Chitosan

*Correspondence:
Franco Furlani
franco.furlani@uniud.it
[1]Department of Medicine, University of Udine, Piazzale Kolbe 4, Udine 33100, Italy
[2]Polytechnic Department of Engineering and Architecture, University of Udine, Via delle Scienze, 206, Udine 33100, Italy
[3]National Research Council of Italy - Institute of Science, Technology and Sustainability for Ceramics - CNR - ISSMC (Former ISTEC), Via Granarolo 64, I – 48018, Faenza(RA), Italy
[4]Italian Liver Foundation - NPO, Area Science Park Basovizza Campus – Bldg. Q SS 14 km 163,5, Trieste 34149, Italy

Introduction

Bone is a complex tissue consisting of cells and bone matrix with a well-defined hierarchically organized architecture and composition. Specifically, cells are mainly represented by osteoblasts, mesenchymal stem cells, osteocytes, and osteoclasts, whereas the bone matrix mainly comprises hydroxyapatite (HA) – an inorganic component – and collagen [1, 2]. The bone tissue is frequently damaged by trauma and diseases, including osteoporosis and cancer, in which the regenerative ability is impaired and needs to be replaced or approaches should be developed to improve bone regeneration [1, 3–9]. In the last decades, intense research on the development of biomaterials suitable for bone regeneration and bone replacement has been done. Some of the most widely used materials are biomimetic ones, i.e. materials able to mimic the structure and composition of native tissues, such as those based on HA, which comprises approximately the 70 wt% of the native bone [1, 10]. Indeed, HA is based essentially on calcium and phosphate ions and its lattice can be doped with different cations, e.g. magnesium and iron, to tune its physical-chemical and biological properties [11–15]. Specifically, doping with iron cations (Fe^{2+} and Fe^{3+}) confers an intrinsic superparamagnetic behavior and the ability to efficiently convey different drugs, e.g. doxorubicin [16, 17]. Specifically, doxorubicin release by iron-doped hydroxyapatite nanoparticles can be finely tuned by the application of an external magnetic field [17]. On the other hand, doping with magnesium cations (Mg^{2+}) – present also in the biologic apatite – reduces HA crystallinity and affects its biodegradation in the human body, finely enhancing its biological activity [18–21]. Indeed, a high crystallinity entails high stability and low biodegradation, whereas an amorphous phase (i.e. without crystalline phases) corresponds to higher surface reactivity, ability to interact with other molecules, and biodegradation, with consequent release of ions for the stimulation of biological activity. HA can be chemically synthesized by different approaches, including sol-gel synthesis and biomineralization, i.e. an approach according to which HA can nucleate on an organic template – e.g. collagen and chitosan – and directly form nanoparticles on polymer molecules generating hybrid biomimetic materials [10, 22]. Specifically, chitosan is a low-toxic and biodegradable natural polymer derived from fungi or deacetylation of chitin – from arthropods exoskeleton and other food waste animal sources – widely used for biomedical applications, especially for the realization of biomaterials for tissue regeneration [23–25]. Indeed, chitosan shares some peculiar features with collagen including a peculiar mechanical performance and a comparable role in the exo- vs. endo-skeleton and flexibility [26]. Additionally, chitosan can be easily modified to tune its physical-chemical properties and cell interaction [27–30].

Recently, it was reported the potential ability of HA, having different morphological properties, to elicit DNA damage and to downregulate genes involved in DNA repair [31]; nevertheless, little is known about the effect of ions-doping and biomineralized structures on the possibility of tuning DNA damage extent and triggering the DNA damage response (DDR) pathway. Indeed, in the previous studies, only native and fluor-doped HA were considered, and slight DNA damage was mainly detected by COMET assay (without deepening the type and mechanism of damage) [31, 32]. In the present study, we report an original method to form HA nanoparticles doped with different ions – i.e. Mg^{2+}, Fe^{2+}, and Fe^{3+} – on chitosan fibers by using a biomineralization process. The physical-chemical and morphological properties of the resulting nanoparticles were assessed by complementary techniques, including X-ray diffraction (XRD) and Scanning Electron Microscopy (SEM). Then, the biological activity of the resulting nanoparticles was investigated by considering both the inorganic nanoparticles (only HA) and hybrid nanoparticles (chitosan biomineralized with hydroxyapatite) using two osteoblasts-like cell lines, i.e. HOBIT (Human OsteoBlast-like Initial Transfectant) and MG63 cells. Specifically, cell metabolism, cell proliferation, oxidative stress, and DNA damage were considered by using complementary techniques to evaluate the possible role of synthetic HA, both ions-doped and biomineralized on chitosan, to modulate cell metabolism and DNA damage.

Materials and methods

Materials

Phosphoric acid (H_3PO_4, 85% pure), calcium hydroxide ($Ca(OH)_2$, 95% pure), magnesium chloride ($MgCl_2 \cdot 6H_2O$, 85% pure), medium molecular weight chitosan (CH) in powder form ([η] = 815 mL/g, which corresponds to a viscosimetric molecular weight equal to 260 000, deacetylation degree > 75%), paraformaldehyde (PFA), Triton X-100, and magnesium chloride were purchased from Merck KGaA (Darmstadt, Germany). Ethanol was from Carlo Erba, Italy. All reagents and chemicals were of high purity grade. Ultrapure water (0.22 mS, 25 °C) was used in all experiments.

Biomineralization of chitosan with ions-doped hydroxyapatite nanoparticles and preparation of hydroxyapatite nanoparticles

To devise biocompatible, biomimetic, and bioactive particles for efficient bone regeneration, two main bio-inspired components, i.e. HA nanoparticles and chitosan, were selected and combined through a wet-chemical synthetic approach. These two components were combined

according to a biomineralization approach – a process according to which it is possible to produce HA nanoparticles directly on polymer chains – and two bioactive ions, i.e. magnesium and iron, were introduced in a wet acid-base neutralization chemical route starting from calcium, magnesium, iron, and phosphate ions (Scheme 1). Specifically, an acidic solution of chitosan was dropped into a basic suspension containing calcium and the appropriate ions (magnesium or iron ions) promoting the formation of doped HA nanoparticles directly on chitosan molecules, and which are named MgHA/CH in the case of magnesium doping, whereas FeHA/CH in the case of iron doping. The same protocol was adjusted to synthesize naked – i.e. without chitosan – HA nanoparticles doped with magnesium (MgHA) or iron (FeHA) and used as a reference for successive characterization. The synthesis conditions - temperature, the ratio between the ions and the rate of addition of the reagents - were set to obtain nanometric particles with low crystallinity, whose visual aspect in the form of powder is reported in Fig. 1A, whereas in the form of nanoparticles suspension is reported in Fig. 1B, confirming the synthesis of aqueous dispersions with different colors, i.e. white in the case of magnesium doping, whereas brown in the case of brown doping, in mineralized and naked particles.

In detail, Mg-doped hydroxyapatite nanoparticles (MgHA) were prepared at environmental temperature by wisely dropping in 90 min 150 mL of an aqueous solution containing 20.63 g of H_3PO_4 (Merck KGaA, Darmstadt, Germany, 85% pure) into a basic suspension consisting of 23.3 g $Ca(OH)_2$ (Merck KGaA, Darmstadt, Germany, 95% pure) and 3.05 g $MgCl_2{\cdot}6H_2O$ (Merck KGaA, Darmstadt, Germany, 85% pure) in 200 mL of water under stirring. The resulting suspension was maintained under stirring for two hours, then left at rest overnight.

1 g of chitosan was solubilized in 200 mL of an aqueous solution containing 1.61 g of H_3PO_4 overnight under stirring. Then the resulting suspension was added to a basic

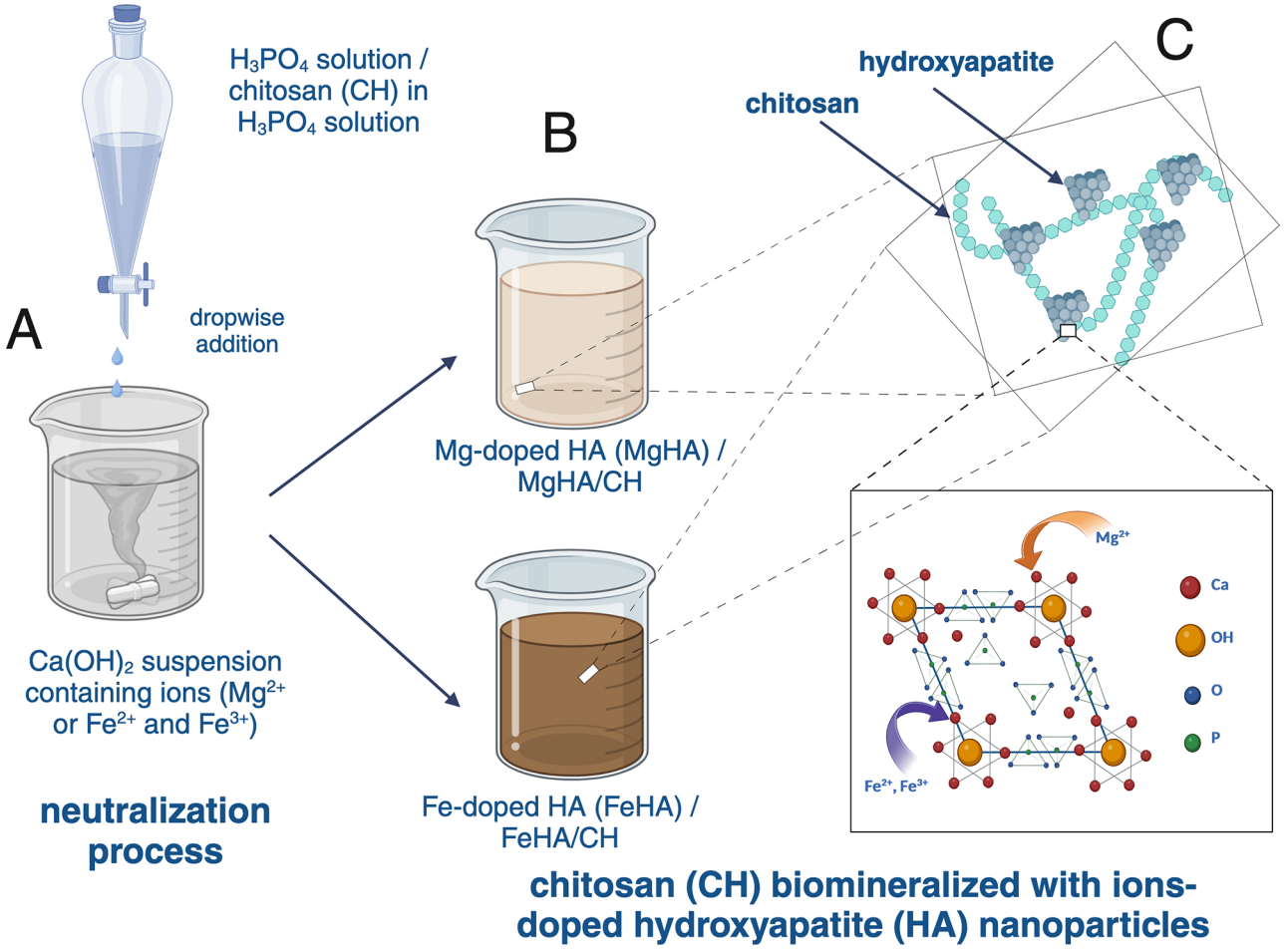

Scheme 1 The schematic synthesis of HA-based nanoparticles and the biomineralization process according to which it is possible to synthesize HA-based nanoparticles on chitosan chains. Specifically, in (**A**), the wet acid-base neutralization of acidic chitosan solution containing phosphate ions in a basic suspension containing calcium ions – and additional doping ions, i.e. Mg^{2+}, Fe^{2+}, and Fe^{3+} – is reported, leading to the biomineralization of chitosan (**B**). In (**C**) the magnification of the schematic formation of hydroxyapatite nanoparticles doped with ions on the chitosan template is reported. Created with Biorender.com

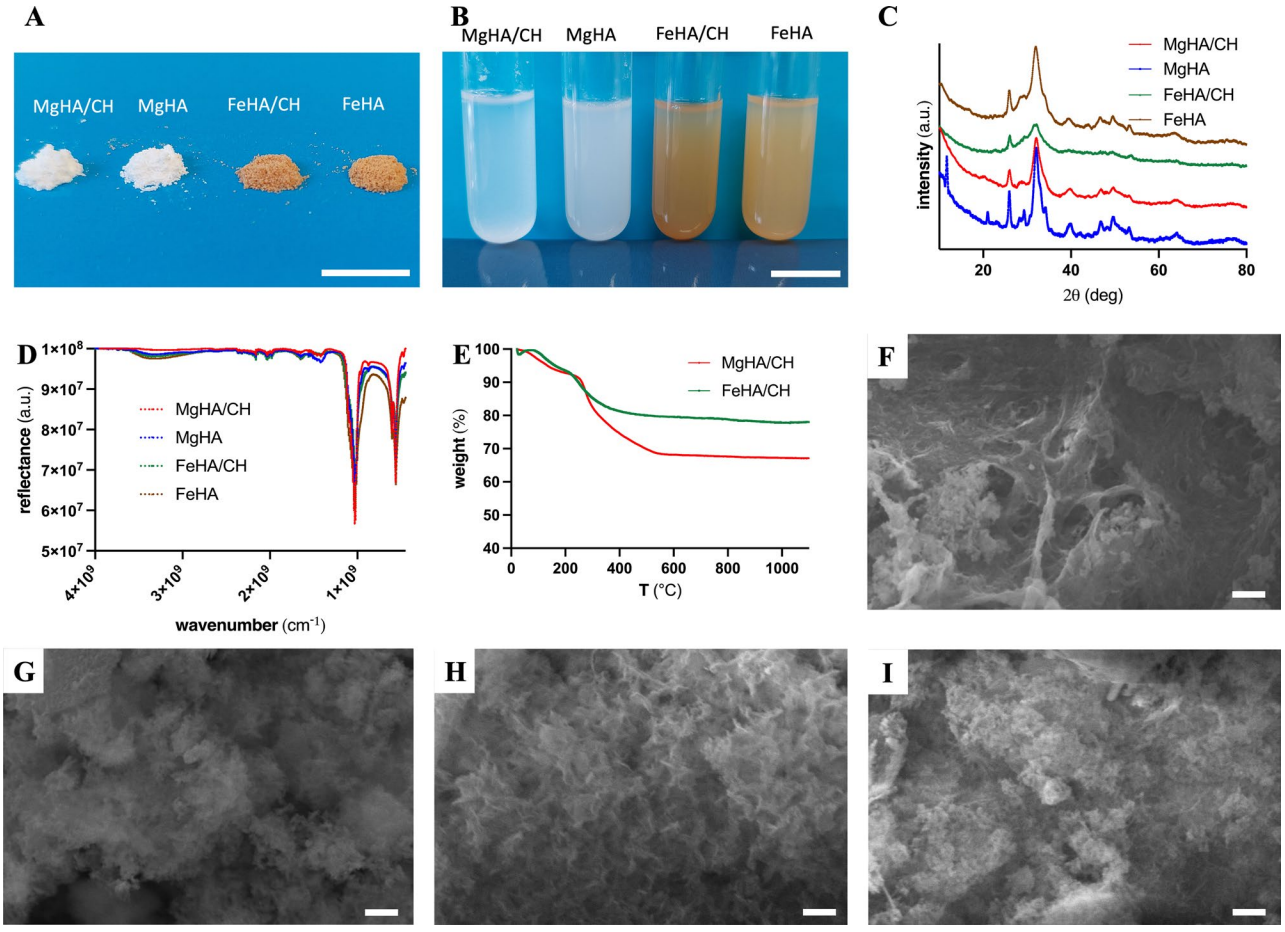

Fig. 1 Physical-chemical and morphological characterization of chitosan biomineralized with HA-based nanoparticles and HA-based nanoparticles. (**A**) Visual analyses of resulting nanoparticles powders; scale: 1 cm. (**B**) Visual analyses of resulting nanoparticles at HA concentration equal to 2 mg/mL in water as a solvent; scale: 1 cm. (**C**) X-ray diffraction (XRD) spectra of resulting nanoparticles. Physical-chemical characterization of hydroxyapatite-based nanoparticles by FTIR-ATR (**D**) and by Thermogravimetric analyses (TGA) (**E**). (**F**), (**G**), (**H**), and (**I**) Scanning Electron Microscopy (SEM) images respectively of MgHA/CH, MgHA, FeHA/CH, and FeHA; in all SEM images scale bar is 400 nm

suspension consisting of 1.81 g $Ca(OH)_2$ and 240 mg $MgCl_2{\cdot}6H_2O$ (Merck KGaA, Darmstadt, Germany, 85% pure) in 200 mL of water under stirring. The resulting pellet consisting of chitosan mineralized with Mg-doped hydroxyapatite nanoparticles (MgHA/CH) was maintained at rest for 2 h.

Fe-doped hydroxyapatite nanoparticles (FeHA) were prepared at 40 °C by wisely dropping in 90 min 150 mL of an aqueous solution containing 20.63 g of H_3PO_4 (Merck KGaA, Darmstadt, Germany, 85% pure) into a basic suspension consisting of 23.3 g $Ca(OH)_2$ (Merck KGaA, Darmstadt, Germany, 95% pure) and 6.02 g $FeCl_2{\cdot}6H_2O$ (Merck KGaA, Darmstadt, Germany, 85% pure) and 8.07 g $FeCl_3{\cdot}6H_2O$ (Merck KGaA, Darmstadt, Germany, 85% pure) in 200 mL of water under stirring. The resulting suspension was maintained under stirring for two hours, then left at rest overnight.

1 g of chitosan was solubilized in 200 mL of an aqueous solution containing 1.61 g of H_3PO_4 overnight under stirring. Two solutions of iron, i.e. 0.47 g $FeCl_2{\cdot}6H_2O$ (Merck KGaA, Darmstadt, Germany, 85% pure) and 0.63 $FeCl_3{\cdot}6H_2O$ (Merck KGaA, Darmstadt, Germany, 85% pure), both of them separately solubilized in 20 mL of water were rapidly added to a basic suspension under stirring at 40 °C consisting of 1.81 g $Ca(OH)_2$ in 200 mL of water. Then the solution of chitosan was slowly added to the basic suspension under stirring at 40 °C and was maintained under stirring for 2 h at the same temperature. The resulting suspension consisting of chitosan mineralized with Fe-doped hydroxyapatite nanoparticles (FeHA/CH) was maintained at rest for 2 h.

Finally, all the resulting suspensions were precipitated by centrifugation and successive resuspension (by sonication) and washed three times. All the resulting slurries were frozen, freeze-dried, and finally sieved with 200 µm mesh before successive characterization.

Inductively Coupled Plasma-Optical Emission Spectrometry

Inductively Coupled Plasma-Optical Emission Spectrometry (ICP-OES, Agilent Technologies 5100 ICP-OES, Santa Clara, USA) was used for the quantitative determination of Mg^{2+}, Ca^{2+}, and PO_4^{3-} ions that constituted the inorganic mineral component. Briefly, 20 mg of each sample were dissolved in 2 mL nitric acid (65 wt%) followed by subsequent sonication and dilution with 100 mL of distilled water.

FTIR-ATR spectroscopy

Fourier transform infrared (FT-IR) spectra of the samples were measured with a Nicolet iS™ 50 FT-IR spectrometer (Thermo Fisher Scientific Inc., Waltham, MA, USA) using the Attenuated Total Reflection (ATR) mode. Each IR spectrum was acquired using a 2 cm^{-1} resolution in a spectral window ranging from 500 to 4000 cm^{-1} with 100 scans.

X-ray diffraction

X-ray diffraction (XRD) patterns were recorded by a Bruker (Karlsruhe, Germany) AXS D8 Advance diffractometer in reflection mode, with CuK radiation (λ = 1.54178 Å) generated at 40 kV and 40 mA and equipped with a Lynx-eye position-sensitive detector. XRD spectra were recorded in the range from 20° to 60° with a step size (2θ) of 0.02° and a counting time of 0.5 s.

Scanning Electron Microscopy (SEM)

Nanoparticles morphologies were investigated by a Zeiss EVO40 Scanning Electron Microscope (SEM) equipped with EDX (Energy-Dispersive X-ray analyses). Samples were mounted on aluminum stubs covered by adhesive carbon tape and gold-sputtered before SEM analyses at 20.0 kV.

Thermogravimetric analyses

Thermogravimetric analyses (TGA) were performed using an STA 449/C Jupiter (Netzsch, Germany) on 10 mg of sample, placed in an alumina crucible under airflow, and brought from room temperature to 1100 °C at a heating rate of 10 °C/minute.

In vitro biological tests

Two different bone cell models were used for in vitro biological tests including human osteoblasts-like cells HOBIT (Human OsteoBlast-like Initial Transfectant, RRID: CVCL_W632) and human osteosarcoma osteoblast-like cells MG63 (ATCC CRL-1427™). HOBIT and MG63 cells were grown using Advanced DMEM/F12 (Gibco, Thermo Fisher Scientific, USA) both supplemented with 10% v/v Fetal Bovine Serum (FBS) and 1% v/v penicillin/streptomycin (100 U/mL-100 µg/mL) at 37 °C in an atmosphere with 5% CO_2. Cells were detached by using trypsin-EDTA (0.25% (w/v) trypsin and 0.03% EDTA) and centrifuged, and the number of viable cells was assessed with a trypan blue dye exclusion test in an automatic CytoSMART Corning (New York, USA) system before seeding in multi-well plates for biological experiments. Cells exposed to H_2O_2 1 mM in OptiMEM (Gibco, Thermo Fisher Scientific, USA) were used positive control cells.

Sterilization of nanoparticle suspension for biological tests

10 mg of ions-doped hydroxyapatite nanoparticles (MgHA and FeHA) were transferred in 1.5 mL Eppendorf tubes with 1 mL of ethanol 70% for 20 min in a sonicating bath. In the case of chitosan biomineralized with ions-doped hydroxyapatite nanoparticles the amount of powder was adjusted (considering the percentage of inorganic components determined by TGA analyses) to have the same amount of hydroxyapatite nanoparticles in all samples; specifically, for chitosan biomineralized with Mg-doped hydroxyapatite nanoparticles, MgHA/CH, 12.8 mg, whereas for chitosan biomineralized with Fe-doped hydroxyapatite nanoparticles, FeHA/CH, 14.9 mg were used. Thereafter, Eppendorf tubes were centrifugated at 12 000 g for 5 min with EBA 12R (Hettich GmbH & Co. KG, Tuttlingen, Germany) to promote the formation of a pellet containing nanoparticles, the supernatant was discarded, 1 mL of sterilized deionized water was added, and nanoparticles were resuspended by using a sonicating bath for 15 min. Finally, nanoparticles were diluted in the appropriate cell culture media to achieve final hydroxyapatite concentrations equal to 200 µg/mL. The composition of cell media was adjusted to have the 10% V/V of deionized water in all samples, including the control.

Cell viability assay

The cellular viability and proliferation of cells were assessed by the PrestoBlue™ Cell Viability Reagent procedure (Invitrogen, Thermo Fisher Scientific, USA) according to the manufacturer's instructions. Briefly, cells were seeded (2.0×10^3 cells/well) in a 96 plate and the next day supernatant was substituted with 100 µL of HA-based nanoparticles diluted in cell culture media. Untreated cells were used as a negative control. Two time points (1 day, 3 days) were evaluated. At the desired timeframe, 10% PrestoBlue Reagent was added for two hours at 37 °C and 5% CO_2 atmosphere in dark conditions under controlled humidity conditions. After incubation, the samples were read at excitation and emission wavelengths of 544 and 590 nm, respectively, by using the BioTek Synergy H1 Multimode Reader (Agilent, USA). At least three replicates for each sample were performed.

Cell counting assay

50,000 cells were seeded in 6-well plates and after letting them overnight at rest, 2 mL of HA-based nanoparticles diluted in cell culture media were added. At the desired timeframe, i.e. after 1, 3, and 7 days of incubation with particles, cells were washed in PBS 1×, detached by using trypsin, and the cell viability were assessed by cell counting with a trypan blue dye exclusion test in an automatic CytoSMART Corning (New York, USA) system.

Clonogenic assay

For clonogenic assay, 1 million cells were seeded in 6-well plates and after 1 day media was replaced with 2 mL of HA-based nanoparticles diluted in cell culture media. After 1 day of incubation with nanoparticles, cells were washed in PBS 1×, detached by using trypsin, and 750 cells were seeded in 6-well plates. Cells were allowed to proliferate and form colonies for 7 days – replacing the media with fresh media every 2–3 days – after which colonies were washed in PBS 1×. Thereafter, colonies were stained by using 800 µL of 10% w/V crystal violet (Merck KGaA, Darmstadt, Germany) in 70% V/V ethanol, washed three times by using deionized water, and let dry. Finally, the number of colonies in each plate was determined by using the ImageQuant TL (Amersham) scanner and its software.

Reactive oxygen species determination

The production of reactive oxygen species by cells was assessed in 96 well-plates (2.0×10^3 cells/well) according to a previously reported protocol with slight modifications [33, 34]. After overnight incubation, the supernatant was discarded and replaced with the nanoparticles diluted in the cell culture media. Cells without nanoparticles were used as a negative control. Reduced glutathione (GSH, Merck KGaA, Darmstadt, Germany) treatment (10 mM), and GSH combined with FeHA/CH, were performed for 1 day as control samples. After 1 day of incubation, supernatants were discarded and cells were washed in PBS 1×, then cells were incubated with 100 µL of CM-H_2DCFDA (ThermoFisher Scientific, USA) 5 µM diluted in OptiMEM medium. Cells were incubated for 30 min in dark conditions, then supernatants were discarded, and cells were washed in PBS 1× and incubated for 30 min in 100 µL of OptiMEM in dark conditions. Finally, multi-well plates were read at excitation and emission wavelengths of 494 and 522 nm, respectively, by using BioTek SynergyH1 (Agilent, USA). At least three replicates for each condition were performed.

Immunofluorescence

80 000 MG63 cells were seeded in 24-well plates and after overnight incubation media was replaced with 500 µL of HA-based nanoparticles diluted in cell culture media. After 1 day of incubation with nanoparticles, cells were washed in PBS 1× and fixed in 4% paraformaldehyde. Cells were permeabilized with 0.25% Triton X-100 in PBS 1× for 5 min. After blocking overnight with 10% FBS in Washing Buffer (Tris HCl 10 mM, pH 7.4, NaCl 150 mM, and Tween 20 0.01%), cells were incubated with the primary antibody anti-γH2A.X (monoclonal antibody, IgG mouse, #05-636 Millipore, Merck, Darmstadt, Germany) diluted 1:500 V/V in blocking solution (10% FBS in Washing Buffer) for 2 h at 37 °C.

Then, cells were incubated with goat Anti-Mouse Alexa Fluor® 555-conjugated secondary antibodies (Abcam, Cambridge, UK) for 1 h at 37 °C. Cells were incubated with DAPI (Thermo Fisher Scientific, USA) 14.3 mM for 5 min at room temperature for nuclear staining. Cells were finally washed and mounted with Mowiol mounting medium with antifading agent 1,4-Diazobicyclo-[2]-octane (DABCO™). Cells were visualized through a Leica TCS SP8 laser-scanning confocal microscope (Leica Microsystems, Wetzlar, Germany) equipped with a stage-top environmental chamber (Okolab, Italy) and operated by Leica Application Suite X (LAS X) 3.5.5 software. Images were collected as z-stacks using a 100 x/1.4 oil immersion objective, a 405 nm diode laser (DAPI excitation), and a tunable white-light laser (λ_{ex}: 555 nm) and are reported as maximum intensity projections. Determination of the fluorescent signal was performed using the FIJI IMAGEJ Software (National Institute of Health, Bethesda, MD, USA).

Western blot analyses

For western blotting analyses, 1 million cells were seeded in 6-well plates. After overnight incubation, media was replaced with 2 mL of HA-based nanoparticles diluted in cell culture media. After 1 day of incubation with nanoparticles, cells were washed in PBS 1×, detached by using trypsin, recovered by centrifugation and the pellet was transferred in a 1.5 mL Eppendorf tube and lysed by using a solution containing 0.1% Triton X-100 and protease inhibitors (dithiothreitol (DTT) 1 mM, phenylmethylsulfonyl fluoride (PMSF) 2.5 mM, protease inhibitor cocktail (PI) 0.001% V/V, NaF 1 mM, and Na_3VO_4 10 mM) in PBS 1× for 10 min in an ice bath, centrifugated at 12 000 g for 30 min at 4 °C with EBA 12R (Hettich GmbH & Co. KG, Tuttlingen, Germany) and stored at -80 °C. The concentration of proteins in the cell lysates (supernatant) was determined by colorimetric Bradford assays (Bio-Rad, Hercules, USA), and 30 µg of proteins were diluted in Laemmli buffer (final loaded volume for each well equal to 20 µL), denatured at 95 °C for 5 min, resolved on 15% SDS/PAGE, transferred onto nitrocellulose membranes (Schleicher & Schuell Bioscience, Dassel, Germany), and incubated overnight with β-tubulin (monoclonal antibody, IgG1 mouse, Merck, Darmstadt,

Germany) 1:2000, PRXSO3 1:1000 (polyclonal antibody, IgG rabbit, Abcam, Cambridge, UK) and γH2AX 1:1000 (monoclonal antibody, IgG mouse, #05-636 Millipore, Merck, Darmstadt, Germany) antibodies. The corresponding secondary antibodies labeled with IR-Dye (goat anti-rabbit IgG IRDye 680 for $PRXSO_3$, goat anti-mouse IgG IRDye 800 for γH2AX, and goat anti-mouse IgG IRDye 680 for β-tubulin) were used (1:10 000) and incubated for 1 h. PageRuler™ Plus Prestained Protein Ladder, 10 to 250 kDa, was used to assess the molecular weight of the corresponding protein. Images were acquired and quantified by using an Odyssey CLx Infrared Imaging System (LI-COR Biosciences). Cells incubated with H_2O_2 1 mM for 10 min in OptiMEM (Gibco, Thermo Fisher Scientific, USA) were used as positive control cells for γH2AX analyses, whereas cells incubated with H_2O_2 1 mM for different timeframes including 2, 4, 8, and 10 min in OptiMEM (Gibco, Thermo Fisher Scientific, USA) were used as positive control cells for $PRXSO_3$ analyses.

Alkaline COMET assay

60 000 HOBIT cells were plated on 24-well plates, and after overnight incubation media was replaced with 2 mL of HA-based nanoparticles diluted in cell culture media. Reduced glutathione (GSH, Merck KGaA, Darmstadt, Germany) treatment (10 mM) was performed for 1 day as control cells. After 1 day of incubation with nanoparticles, cells were washed in PBS 1×, detached by using 50 µL of trypsin for 10 min, recovered by pipetting and adding 200 µL of complete media. The pellet was mixed with 1 mL of low melting point agarose 1% w/V (LE GQ Agarose, MBI Fermentas, USA) in PBS 1× pre-heated at 40 °C. One milliliter of the mixture was applied on a SuperFrost Menzel (Thermo Scientific, USA) glass coverslip pre-coated with a thin layer (800 µL) of normal melting point agarose 1% w/V (Merck KGaA, Darmstadt, Germany) in deionized water (let dry at 4 °C overnight). Cells were then lysed with cold alkaline lysis buffer (NaCl 2.5 M, EDTA disodium salt 100 mM, Tris base 10 mM, 1% DMSO, 1% Triton X-100; pH 10.5) for 1 h at 4 °C. Next, cells were transferred to an electrophoretic cell (Hoefer supersub, Hoefer Inc, USA) and covered with alkaline electrophoresis buffer (300 mM NaOH, 1 mM EDTA, 1% DMSO; pH>13) for 30 min for the DNA to denature. DNA electrophoresis was carried out at 25 V and 300 mA for 25 min at room temperature. Coverslips were washed with neutralization buffer (Tris-HCl 500 mM, pH 8.1) for 5 min at room temperature three times and let dry at 60 °C for 2 h. DNA was then stained with 1 mL of SYBR™ Gold Nucleic Acid Gel Stain (Thermo Fisher Scientific, USA) solution 1× (diluted 1:10 000 in deionized water) for 30 min at room temperature in the dark and let dry at 60 °C for 2 h. Leica TCS SP8 laser-scanning confocal microscope (Leica Microsystems) was used for comet analysis. The olive tail moment was measured by the IMAGEJ Software (National Institute of Health, Bethesda, MD, USA) plugin OPENCOMET.

Statistical analysis

Statistical analysis and graph elaboration were performed using GraphPad Prism 10 (GraphPad Software, San Diego, CA). One-way ANOVA (analysis of variance) was performed followed by Dunnett *post hoc* tests to evaluate differences among different groups and control or Tuckey *post hoc* tests to evaluate differences among all groups. Differences were considered significant for p-values less than 0.05.

Results and discussion

Physical-chemical characterization of chitosan biomineralized with ions-doped hydroxyapatite nanoparticles

In the synthesis, magnesium and iron ions were introduced to boost the bioactivity – in terms of biocompatibility and cell-regenerative ability – of the resulting hydroxyapatite (HA) [16, 19, 22]. According to ICP-OES analyses (Table 1) the [Ca+Mg]/P molar ratio in MgHA/CH and MgHA resulted close to the stoichiometric HA, in which the Ca/P molar ratio is equal to 1.66, whereas the Mg/Ca molar ratio resulted respectively equal to 6% and 3%, i.e. close to the amount present in the biological apatite in our bones, therefore it can be considered biomimetics [19]. In the case of FeHA/CH and FeHA, the [Ca+Fe]/P molar ratio resulted close to the stoichiometric HA (Ca/P molar equal to 1.66), whereas the Ca/P was reduced compared to magnesium-doped particles, confirming the high percentage of iron ions within HA lattice, respectively equal to 24 and 31%. Consequently, for both ions doping, and for biomineralized and naked particles, it was possible to confirm by ICP-AES, the successful doping of HA lattice and partial replacement of calcium with magnesium and iron (Scheme 1). Similar

Table 1 Characterization of molar ratio and ions percentage (Mg/Ca) within HA-based nanoparticles by ICP-AES, crystallinity degree by XRD, and the organic content by thermogravimetric analyses

Sample	Ca/*P*	[Mg (or Fe) + Ca]/*P*	Mg (%)	Fe (%)	Crystallinity degree (%)	Organic content (w/w %)
MgHA/CH	1.61	1.70	6	/	8	33
MgHA	1.56	1.61	3	/	12	/
FeHA/CH	1.34	1.67	1	24	/	22
FeHA	1.23	1.62	1	31	/	/

results were previously reported for FeHA and collagen biomineralized with FeHA, confirming the synthesis of iron-doped HA particles on the polymer template [35]. Additionally, similar iron doping on HA particles was reported as endowed with the ability to be used as an agent for magnetic and nuclear in vivo imaging and to covey an anticancer drug, i.e. doxorubicin [17, 36]. On the other hand, magnesium-doped particles with comparable ion doping resulted in excellent biocompatibility in vivo in an animal model [19].

The resulting particles were analyzed by X-ray diffraction (XRD) (Fig. 1C), according to which it was possible to detect the common pattern of analogous nanosystems produced through wet chemistry route [37–40], as well as natural HA present in bones [19], confirming the successful synthesis of HA – without the presence of other crystalline phases [41] – in all samples; additionally, the successful synthesis of HA was also confirmed by FTIR-ATR (Fig. 1D) analyses, according to which the classic peaks pattern was detected.

Considering the XRD intensity of the classic peaks corresponding to HA (Fig. 1C), it was possible to investigate the crystallinity of the resulting particles. The intensity of peaks was low compared to the stoichiometric HA, suggesting the formation of HA with nanosized crystallites, therefore the resulting apatite phase was referred to as HA nanoparticles. The relation determined the crystallinity grade (X_c) of the apatite phase: $X_c \sim 1-(V_{112}/_{300} / I_{300})$ where I_{300} is the intensity of (300) reflection and $V_{112}/_{300}$ is the intensity of the hollow between (112) and (300) reflection which completely disappears in non-crystalline samples [18, 19]. In MgHA, the crystallinity degree resulted to be equal to 12%, whereas in MgHA/CH the crystallinity degree resulted to be equal to 8% (Table 1) suggesting that the presence of chitosan reduced the crystallinity of apatite, as previously reported for other polymers, e.g. gelatin [10]. In the case of iron doping (FeHA and FeHA/CH), it was not possible to determine the crystallinity of samples suggesting that the partial substitution of calcium with iron further reduced the crystallinity promoting the formation of amorphous HA nanoparticles. Indeed, the synergistic effect of the low (room) temperature of the synthesis and the presence of doping ions inhibited the crystallization process inducing the formation of small apatite nuclei.

The thermal behavior of the nanostructures was then investigated by ThermoGravimetric Analyses (TGA) (Fig. 1E), according to which it is possible to estimate the percentage of the organic component, i.e. chitosan, within particles. Indeed, chitosan tends to degrade at temperatures higher than 600 °C, and only the inorganic component, i.e. HA, remains stable in such conditions and can be quantitatively determined. According to this approach, the percentage of chitosan within MgHA/CH and FeHA/CH resulted respectively equal to 33% and 22% w/w (Table 1). In MgHA/CH the percentage of the organic component was comparable to the theoretical percentage used during the synthesis (equal to 30%), whereas in FeHA/CH the chitosan fraction was reduced and this result can be explained by considering the different temperature synthesis conditions; indeed, in FeHA/CH synthesis was performed at 40 °C, and that temperature in basic conditions promoted a partial degradation of chitosan, which increased its solubility and partially reduced its precipitation during the acid-base neutralization procedure. Similar results were previously reported for collagen biomineralized with FeHA, confirming the effective biomineralization of iron-doped HA particles on the organic template [35].

Finally, the morphological characterization of particles was performed by Scanning Electron Microscopy (SEM) analyses at high magnification, according to which it was possible to determine the partial aggregation of HA nanoparticles in all samples (Fig. 1F, G and H, and 1I), and the presence of small flakes in MgHA/CH and FeHA/CH associated to the presence of chitosan on which apatite nuclei can form, confirming the effective biomineralization of chitosan with ions-doped HA nanoparticles. Similar results were previously reported for chitosan biomineralized with non-doped HA nanoparticles, suggesting a limited impact of ions-doping on the microarchitecture of resulting materials [38].

Effects of HA nanoparticles on osteoblast cell lines metabolism and redox status

Considering the potential of these nanoparticles for bone regeneration and bone replacement, their molecular interaction with bone cells was investigated. Specifically, two human cell models were selected that are HOBIT cells, osteoblasts able to recapitulate primary osteoblasts function due to their biochemical and morphological properties [42–46], and MG63, one of the most widely used cell models for bone studies and considered as endowed with osteoblasts-like features [47–49]. Osteoblasts-like cells were selected due to their high proliferative ability and low genomic variability, therefore suitable for the early detection of possible DNA damage [46]. On the other hand, bone marrow stem cells (BMSCs) display low proliferation and are subjected to high differences between different donors in the gene expression pattern [50, 51]. Considering that the biomineralization of chitosan with ions-doped HA can affect cell function, cells were incubated with HA-based nanoparticles doped with magnesium (MgHA/CH) and iron ions (FeHA/CH) and with the free HA-based particles (MgHA and FeHA, respectively) at the same corresponding concentration as those used to functionalize chitosan. Indeed, using the free HA particles makes it possible to decouple the

biological activity of the precursors from the biomineralized chitosan particles, and untreated cells were used as control samples. After the incubation with particles, cell metabolism and cell proliferation were investigated by PrestoBlue assay – according to which the fluorescence intensity is proportional to the cell metabolic activity – and cell counting, respectively (Fig. 2). Considering the HOBIT metabolic activity, after 1 and 3 days, at both time-frames chitosan biomineralized with iron-doped HA (FeHA/CH) enhanced cell metabolism, whereas other nanoparticle types (MgHA/CH, MgHA, and FeHA) did not significantly affect cell metabolism suggesting that HA-based particles can be considered as safe materials (Fig. 2A). In MG63, a similar response was detected (Fig. 2B). Specifically, after 3 days, FeHA/CH enhanced cell metabolism and iron-doped particles without chitosan (FeHA) partially reduced cell metabolism, whereas after 1 day both iron-doped particles did not significantly alter cell metabolism. On the other hand, chitosan biomineralized with magnesium-doped HA (MgHA/CH) and the naked particles (MgHA) enhanced cell metabolism at both timeframes. Considering the cell number, upon 1 day of incubation with particles, none of the cell lines were affected, whereas after 3 days a significant decrease in the cell number was detected in both cells treated with different particle types (Fig. 2C and D). The reduction of cell number after 3 days could be correlated to the presence of a high number of particles present inside the well of the plate which could sterically limit the cell mobility and proliferation. Considering the different trends in cell metabolism and cell number, the increased fluorescence detected by PrestoBlue assay in most particles-treated cells indicates a change in cell metabolism in osteoblasts and osteoblasts-like cells, particularly in cells treated with FeHA/CH. In that case, these data suggest that due to the amorphous state of iron-doped particles, these particles can be metabolized by cells and the presence of chitosan can improve the cell interaction and internalization – and therefore cell metabolism – as already detected for other systems-based on chitosan [52]. On the other hand, chitosan biomineralized with magnesium-doped particles displayed similar biological activity to naked (i.e. without chitosan) particles suggesting that the presence of particles with low crystallinity and with a magnesium content comparable to the native bone can be easily metabolized by cells without significantly affecting their metabolic fate. A comparable increase in osteoblasts metabolism was previously reported for other ions-doped HA-based materials, i.e. strontium-doped cement, and was attributed to cell osteogenic differentiation and proliferation, albeit the cell number was not quantitatively assessed [14]. Similar results, i.e. an increase in pre-osteoblast metabolism after three days of treatment, in the presence of comparable concentrations of recombinant collagen particles mineralized with FeHA, were previously reported [53]. Different findings, i.e. a decrease in cell metabolic activity upon the incubation with HA nanoparticles, were previously reported for mouse colorectal cancer cells and were attributed to the peculiar cell type behavior [54]. On the other hand, collagen biomineralized with similar concentrations on magnesium-doped HA nanoparticles resulted as endowed with good biocompatibility towards similar pre-osteoblast cells [55]. Consequently, considering the previously mentioned results, the slight decrease in cell number reported for the present experiment can also be attributed to cell differentiation, as previously reported for collagen biomineralized with FeHA [56]. Specifically, in the presence of iron-doped hydroxyapatite nanoparticles, MG63 cells were able to promote the expression of genes correlated to the osteogenic differentiation, i.e. Collagen type I and ALP [56].

Considering that particles can be metabolized and the ions within the HA lattice – especially iron – can affect the cells' metabolic activity, especially the production of Reactive Oxygen Species (ROS), this latter aspect was investigated by using H2DCFDA as substrate – able to produce a fluorescent signal proportional to ROS production – and deepen by investigating the sulfonation of Peroxiredoxin (Prx) into PrxSO3 [57–59] – an oxidation-induced protein modification of redox-active Cys-residues in the case of cellular oxidative stress condition which endows Prx to function as very sensitive H_2O_2 sensors [60] – by Western blot analyses, after 1 day of incubation with particles. Considering the ROS production, a significant increase in ROS production was detected only in HOBIT cells treated with FeHA/CH (Fig. 2E), whereas no difference in ROS production was detected in the case of other particle types and in MG63 cells (Fig. 2F). On the other hand, GSH was able to limit ROS production – both alone and also in combination with FeHA/CH – ROS production. These data confirm the ability of chitosan to improve nanoparticle internalization and metabolism, the ability of GSH to limit ROS production, and the ability of iron from nanoparticles to participate in the Fenton reaction, able to promote ROS production [61, 62]. An increase in ROS production in the presence of HA particles within a polymeric network was previously reported in pre-osteoblasts, albeit the authors did not report any biological explanation about the phenomenon [63].

Taking into account the possible modification of Prx in the case of oxidative stress, no significant presence of the modified protein was detected after the incubation with all nanoparticle types and both cell models (Fig. 2G and H) suggesting that nanoparticles are not able to produce a ROS amount sufficient to promote the sulfonation of Prx, if compared to H_2O_2 treatment– used as positive

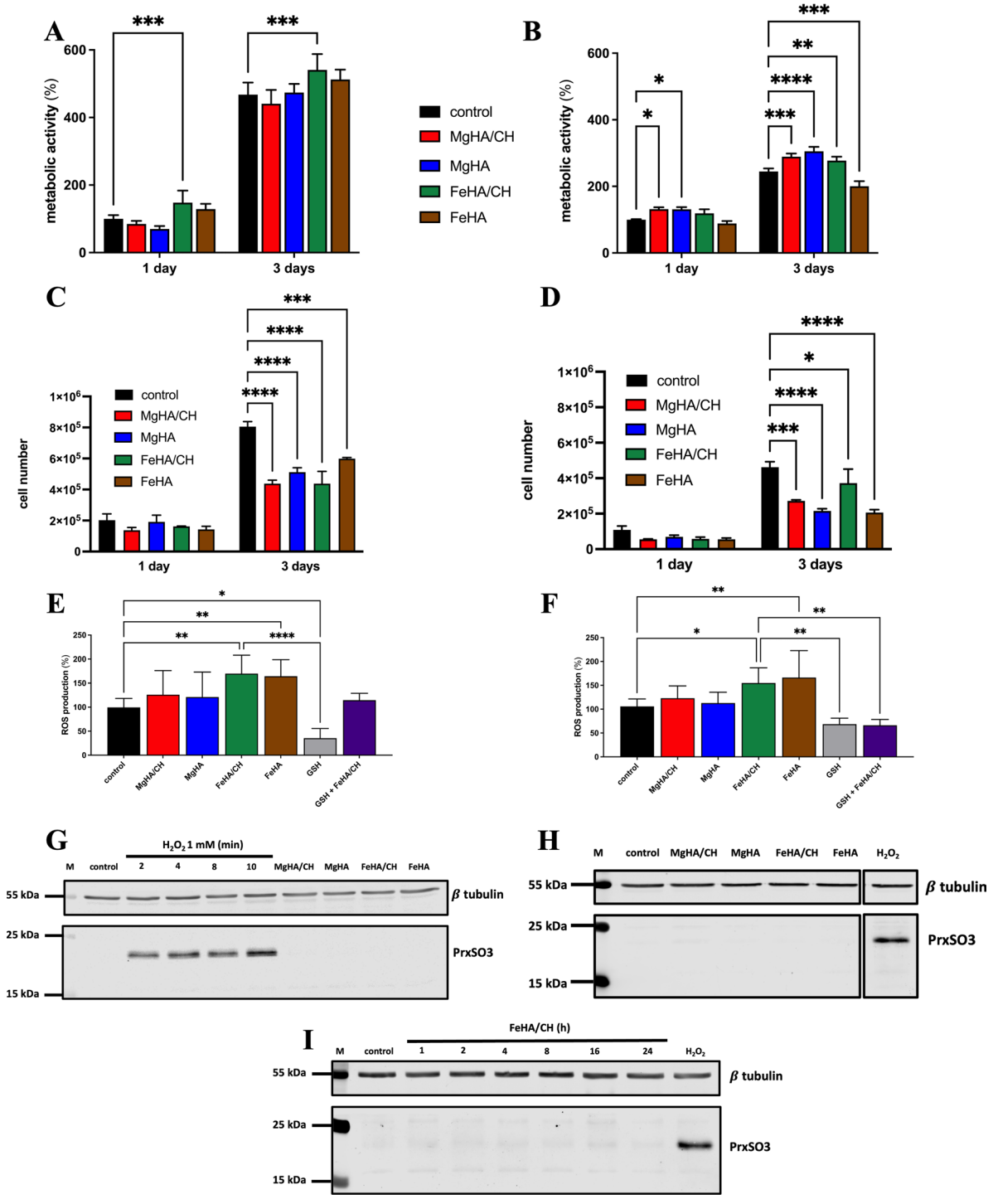

Fig. 2 Effects of HA nanoparticles on osteoblasts metabolism and redox activity. Metabolic activity by PrestoBlue assay of HOBIT (**A**) and MG63 (**B**) after 1 and 3 days of incubation with particles. Fold change values relative to untreated cells are shown. Values are mean ± SD. The resulting *p*-value is indicated (*$p < 0.05$; **$p < 0.01$; **$p < 0.001$; ****$p < 0.0001$) ($n = 3$). Cell number determined by cell counting of HOBIT (**C**) and MG63 (**D**) after 1 and 3 days of incubation with particles. Fold change values relative to untreated cells are shown. Values are mean ± SD. The resulting *p*-value is indicated (*$p < 0.05$; **$p < 0.01$; **$p < 0.001$; ****$p < 0.0001$) ($n = 3$). ROS production was determined using H2-DCFDA as a substrate of HOBIT (**E**) and MG63 (**F**) after 1 day of incubation with particles and/or with reduced glutathione (GSH). Fold change values relative to untreated cells are shown. Values are mean ± SD. The resulting *p*-value is indicated (*$p < 0.05$; **$p < 0.01$; **$p < 0.001$; ****$p < 0.0001$) ($n = 3$). PrxSO3 was determined by Western blot of HOBIT (**G**) and MG63 (**H**) after 1 day of incubation with particles and with H_2O_2 1 mM for different timeframes; specifically, HOBIT cells were incubated with H_2O_2 1 mM for 2, 4, 8 and 10 min, whereas MG63 for 10 min. Tubulin was used to normalize PrxSO3 levels. (**I**) PrxSO3 was determined by Western blot analyses of HOBIT after incubation with FeHA/CH particles for different timeframes (1, 2, 4, 8, 16, and 24 h) and with H_2O_2 1 mM for 10 min. Tubulin was used to normalize PrxSO3 levels. In all tests, the particle concentration was adjusted to have the same HA concentration in all samples

control for the Prx activation – in which a PrxSO3 modification was proportional to the time of the stimulus. The possible modification of Prx was investigated also after the incubation at earlier timeframes – i.e. 1, 2, 4, 8, 16, and 24 h – with FeHA/CH, confirming the not detectable activation of PrxSO3 (Fig. 2I).

Effects of HA nanoparticles on osteoblasts DNA damage

Considering the potential ability of ROS to elicit DNA damage, this latter aspect was investigated after exposure to different nanoparticles for 1 day. Specifically, single- and double-strand breaks, and alkali labile sites were investigated by alkaline COMET analyses [64]. In the latter tests, cells treated with reduced glutathione (GSH) – a well-known antioxidant agent [65, 66] – were used to limit DNA damage. As shown in the representative comet cell analyses, in H_2O_2-treated cells the typical DNA comet was detected (Fig. 3A). By measuring the olive tail moment, all particle types, excluding iron-doped naked particles (FeHA), promoted a significantly higher rate of DNA damage accumulation, whereas GSH reduced oxidative stress and consequently DNA damage, as expected (Fig. 3C). A comparable increase in tail intensity was previously reported also for haemocytes from an animal model, i.e. Drosophila melanogaster, exposed to HA nanoparticles [31]. Additionally, a slight increase in tail intensity was previously reported for fibroblasts (Chinese hamster V79 cells) exposed to eluate from fluor-doped HA [32].

Additionally, the phosphorylation of histone H2AX on Ser^{139} generating γH2AX, a marker of DNA damage response, was investigated [67–71]. This histone modification was quantitatively assessed by Western blot and immunofluorescence analyses. Considering γH2AX foci by immunofluorescence analyses (Fig. 3B and D), a comparable trend to what was detected by Western blot analyses was observed (Fig. 3E and F). Specifically, in the presence of both chitosan biomineralized HA particles (MgHA/CH and FeHA/CH), a significantly higher rate of DNA damage accumulation was detected, whereas in the presence of naked particles (MgHA and FeHA) no difference in the DNA damage was detected. Additionally, as shown in the representative comet cell analyses, in H_2O_2-treated cells the typical γH2AX foci were detected (Fig. 3B).

On the other hand, considering the Western blot analyses, both chitosan biomineralized with HA particles (MgHA/CH and FeHA/CH) and iron-doped naked particles (FeHA) significantly enhanced γH2AX formation in HOBIT and MG63 cells (Fig. 3E, F, G and H), whereas magnesium-doped naked particles (MgHA) did not significantly affect the H2AX modification. Additionally, in both cell lines, FeHA/CH particles promoted the highest γH2AX formation, therefore these particles were selected to investigate the time-response of γH2AX formation, incubating cells for different timeframes with the particles (Fig. 3I). According to this approach, a progressive increase in modification of H2AX – with a maximum activation after 16 h, and a good activation after 24 h – was detected.

Considering the potential ability of DNA damage to impair cell growth, the cell colony formation assay was performed. Specifically, cells pre-incubated with particles were left to grow for 7 days, and the ability of single cells to grow and form visible colonies was investigated (Fig. 4A and B). According to this test, it was possible to appreciate the ability of HOBIT and MG63 cells to grow in all considered conditions, albeit the number of resulting colonies was reduced in cells pre-incubated with iron-doped particles and, only in MG63, treated with MgHA/CH (Fig. 4C and D). These changes correlate to an increase in colonies' average intensity after exposure to MgHA and iron-doped particles (Fig. 4E and F) and confirm the ability of particles to elicit a change in cell metabolism – previously reported in Paragraph 2.3 – and to DNA damage, which affects the cell growth. A slight decrease in colony growth was previously reported for Chinese hamster fibroblast (V79 cells) exposed to non-doped and fluor-doped HA and the higher toxicity detected for fluor-doped particles was attributed to the release of the toxic ion fluoride [32].

Collectively, these data indicate that FeHA/CH particles are endowed with the ability to promote DNA damage and this activity can be attributed to the amorphous state of particles, which can be metabolized by cells making available iron ions, able to improve ROS production (Fig. 2E) and the ability of chitosan to enhance the cell internalization (Scheme 2) – and possible interaction with DNA – as already detected for other systems based on chitosan [52, 72–75]. DNA damage can be due to the direct interaction of HA and chitosan with DNA due to the presence of phosphate ions able to electrostatically interact with DNA and due to the ability of positively charged chitosan to efficiently interact with the negatively charged nucleic acids, including miRNAs and DNA [52, 72–75]. This latter ability is widely exploited also for cell transfection [69–72]. Therefore, the DNA damage detected in cells treated with FeHA/CH particles can be attributed to ROS production, but also ROS-independent mechanisms in the DNA damage should be considered, especially with other particle types. Specifically, also MgHA/CH particles promoted DNA damage and this ability can be attributed to the ability of chitosan to enhance the cell internalization and possible interaction with DNA, as already reported for other systems based on chitosan [76–78]. On the other hand, the limited DNA damage detected for MgHA particles suggests that the presence of particles with low crystallinity and with a

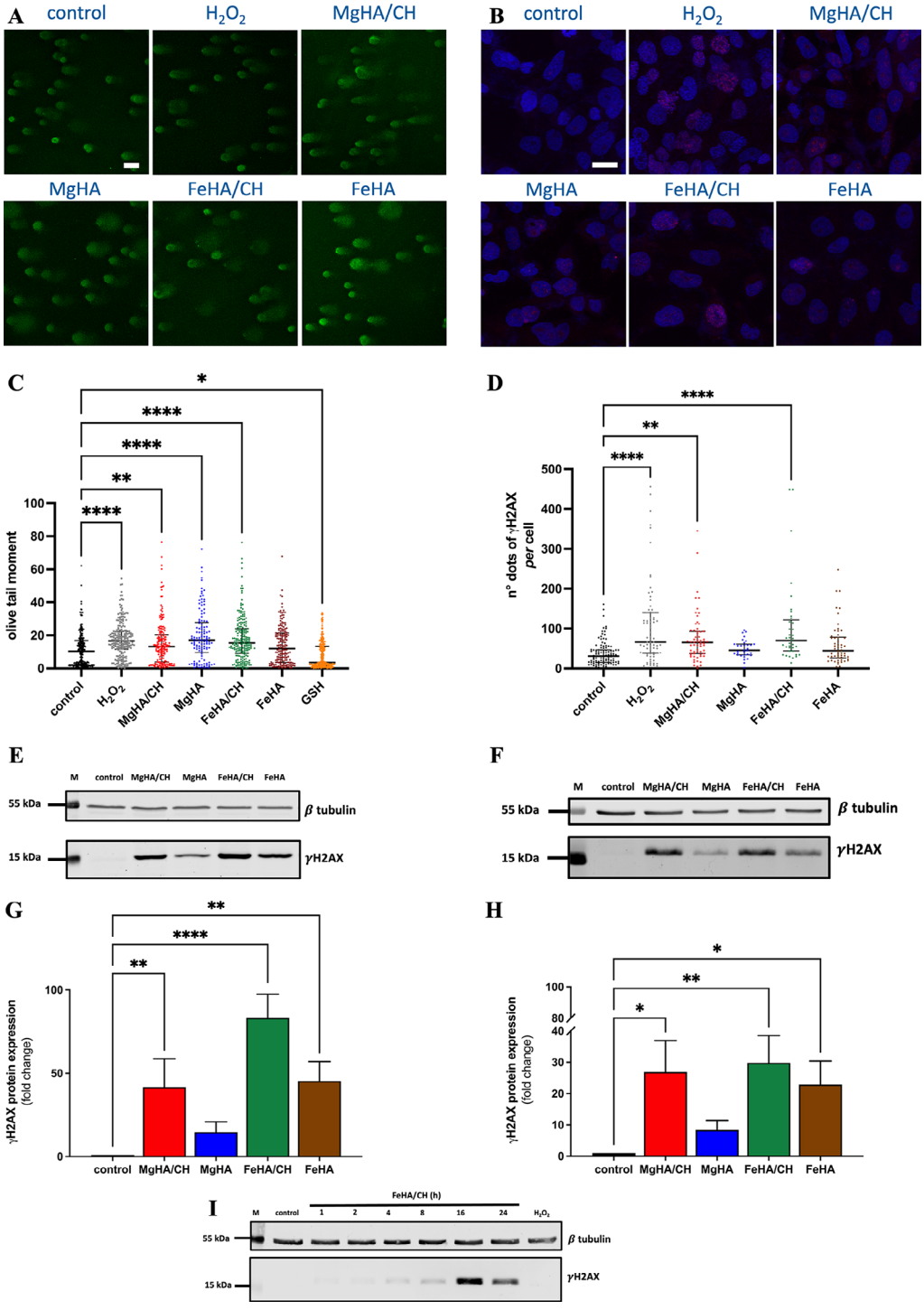

Fig. 3 Effects of HA nanoparticles on osteoblasts DNA damage after 1 day of incubation with particles. (**A**) COMET assay of HOBIT cells after 1 day of incubation with particles and with H_2O_2 as a positive control. The scale bar is 100 µm. (**B**) Immunofluorescence analyses of γH2A.X foci (red). Nuclei were visualized with DAPI (blue). The scale bar is 20 µm. (**C**) Confocal microscopy determined the number of olive tail moments per cell of randomly selected HOBIT cells after incubation with particles and GSH for 24 h and with H_2O_2 300 µM for 15 min. Individual values are shown as mean ± SD. The resulting *p*-value is indicated (*$p < 0.05$; **$p < 0.01$; ****$p < 0.0001$). (**D**) The number of γH2AX dots *per* cell of MG63 cells determined by confocal microscopy after incubation with particles and with H_2O_2 1 mM for 30 min. The resulting *p*-value is indicated (**$p < 0.01$; ****$p < 0.0001$). γH2AX determined by Western blot of HOBIT (**E**) and MG63 (**F**). Tubulin was used to normalize γH2AX levels. Densitometric analysis of γH2AX protein expression of HOBIT (**G**) and MG63 (**H**) normalized to tubulin. Fold change values relative to untreated cells are shown. Values are mean ± SD. The resulting *p*-value is indicated (*$p < 0.05$; **$p < 0.01$; ****$p < 0.0001$) ($n = 3$). (**I**) γH2AX determined by Western blot of HOBIT after incubation with FeHA/CH particles for different timeframes (1, 2, 4, 8, 16, and 24 h) and with H_2O_2 1 mM for 10 min

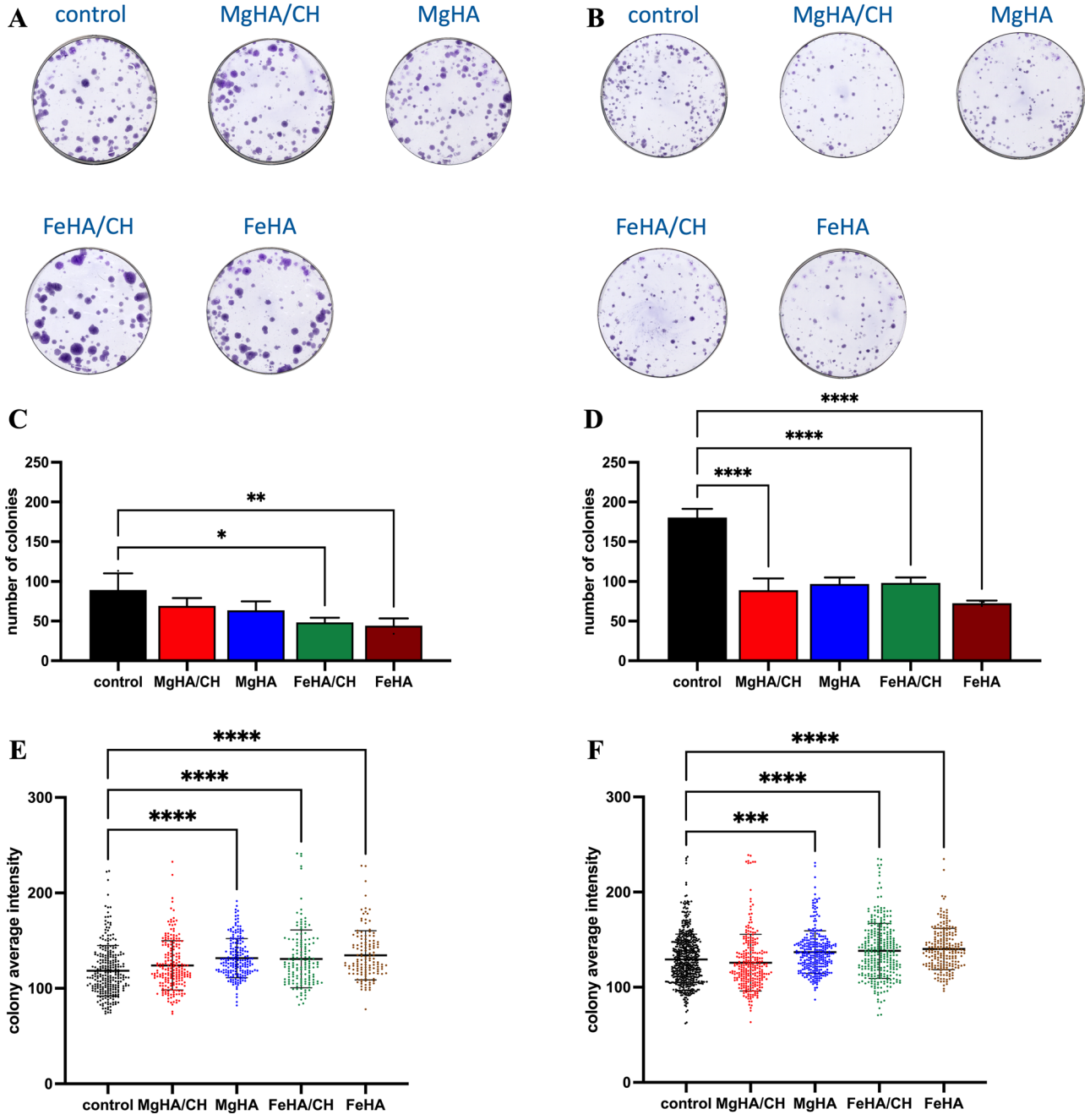

Fig. 4 Effects of HA nanoparticles on osteoblasts colony formation. (**A**) Cell colony assay of HOBIT cells after 7 days. (**B**) Cell colony assay of MG63 cells after 7 days. Analyses of colony formation rates and colony average intensity for HOBIT (**C** and **E**) and MG63 **D** and **F**). Cells were incubated with particles for 1 day, then detached, counted, and plated; the number of formed cell colonies was counted 7 days after seeding. Individual values are shown as mean ± SD. The resulting *p*-value is indicated (*$p < 0.05$; **$p < 0.01$; ****$p < 0.0001$)

magnesium content comparable to the native bone can be easily metabolized by cells without significantly affecting the DNA damage. Indeed, the crystallinity of particles affects the possible biodegration by cell metabolism, governing the presence of ions within cells. Iron-doped particles resulted in being amorphous, i.e. without any crystalline phase, leading to cell metabolism, the production of reactive oxygen species, and DNA damage. On the other hand, magnesium-doped particles showed a moderate crystallinity range (8–12%) and this entals a reduced biodegration by cell metabolism, and consequently a moderate magnesium ions release. Additionally, the different DNA damage types should be considered. Indeed, double-strand DNA damage can be correlated to toxic stress (e.g. ionizing agents), whereas single-strand DNA damage can be correlated to replicative stress [79, 80].

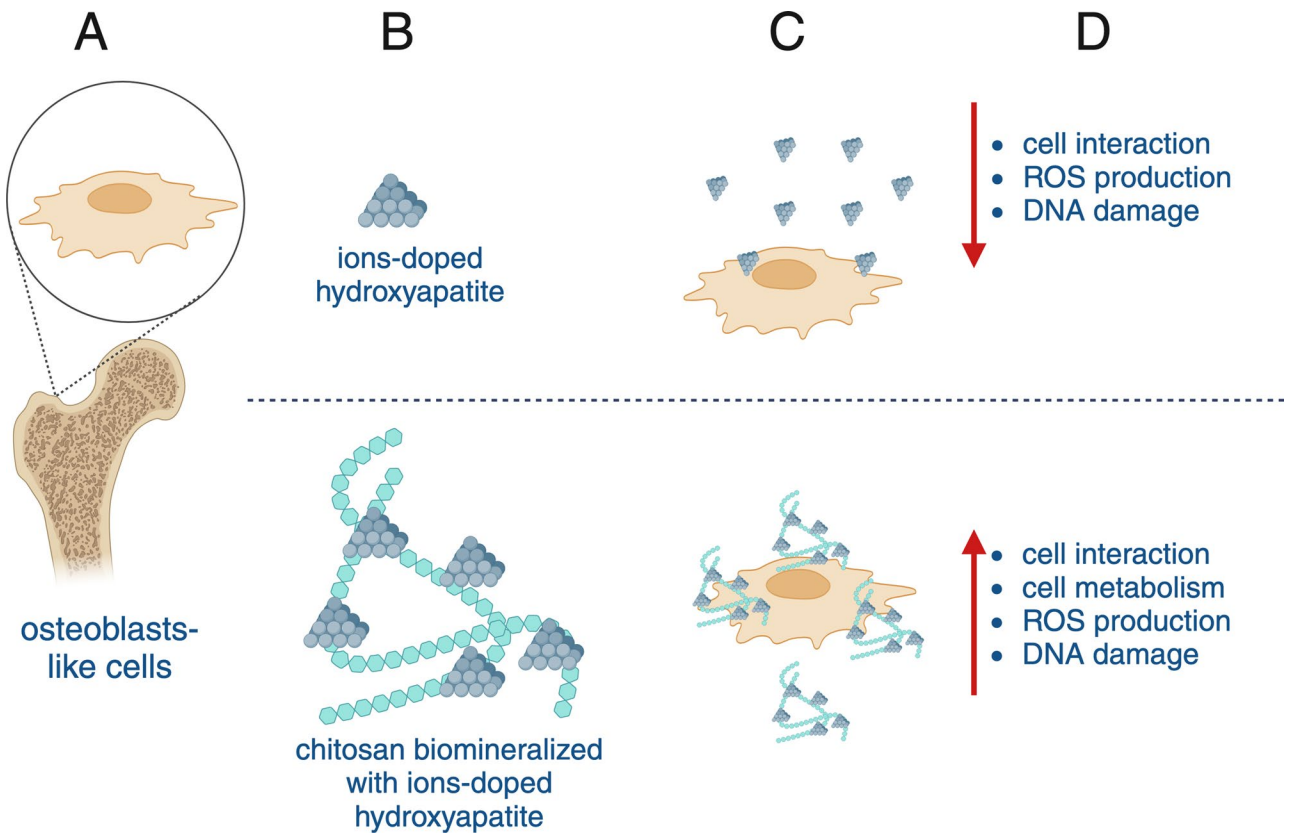

Scheme 2 Sketchy representation of the interaction between cells and nanoparticles and the resulting molecular effects on cells. Specifically, osteoblasts-like cells (**A**) were incubated with ions-doped hydroxyapatite nanoparticles or chitosan biomineralized with ions-doped hydroxyapatite nanoparticles (**B**). Ions-doped hydroxyapatite nanoparticles slightly interacted with osteoblasts leading to a low impact on cell metabolism, ROS production, and DNA damage, whereas chitosan biomineralized with ions-doped hydroxyapatite nanoparticles were able to have a higher interaction with osteoblasts (**C**) leading to an increase in cell metabolism, ROS production, and DNA damage (**D**). Created with Biorender.com

Collectively, taking into account: *i*) the ability of FeHA/CH to promote ROS-production and DNA damage, *ii*) the ability of particles to promote DNA-damage and trigger the DNA-damage response (DDR), *iii*) the previously reported data about the ability of FeHA particles to bind and efficiently convey different drugs such as doxorubicin [17], *iv*) the superparamagnetic properties of FeHA, which can be used to remotely direct particles to the target site and for hyperthermic applications [16], *v*) the ability of chitosan to efficiently bind and convey into cells drugs and nucleic acids [72, 81], *vi*) the recently reported systems based on HA for anticancer treatment [54, 82, 83], the system proposed in the present paper based on chitosan biomineralized with iron-doped HA can be proposed as a drug delivery system, especially to devise cancer treatments. The presence of chitosan, in combination with nanoparticles, seems to enhance the DNA damage suggesting the ability of chitosan to favor the nanoparticles' internalization due to the intrinsic ability of chitosan to be engulfed in cells [29] and this can lead to a higher production of reactive oxygen species, leading to DNA damage. The DNA damage should also be considered in forthcoming studies with modified hydroxyapatite-based particles. Specifically, in the case of materials intended for anticancer therapy, the DNA damage could be further increased by doping hydroxyapatite with toxic ions and the conjugation with anticancer drugs, e.g. doxorubicin. Additionally, considering the recently reported results about the positive immune activation in cancer induced by magnesium-doped HA [20], also the magnesium-doped particles developed in the present study can be proposed as an innovative system for cancer treatment.

In the present contribution, we have proposed a method for chitosan biomineralization with biomimetic magnesium and iron-doped HA particles. The resulting particle properties – e.g. organic content and amount and type of doping ions – can be finely tuned, resulting in a versatile platform to tune cell behavior. Specifically, all particles – considered in this paper – can modify cell metabolism, and chitosan biomineralized with magnesium and iron-doped particles as well as iron-doped HA particles promote DNA damage, whereas the particles with the highest similarity to the native bone, i.e. magnesium-doped HA particles, do not significantly elicit DNA

damage. Indeed, the DNA damage can be mainly attributed to a ROS-independent mechanism.

This system results in a platform that can be easily modified in terms of the type and amount of polymeric template as well as the type and amount of ions doping to tune its bioactivity. On this basis, such nanoparticles are promising for application in medicine, particularly in bone tissue engineering as a bioactive bone filler, or as a drug delivery carrier due to the highly active surface of the HA nanoparticles which can be functionalized with drugs or growth factors. Furthermore, iron-doped particles can be considered also as potential agents for magnetic and nuclear in vivo imaging. Specifically, it was reported that iron-doped hydroxyapatite (FeHA) displayed a higher contrast enhancement in magnetic resonance imaging (MRI), and had a longer endurance in the liver than Endorem (dextran-coated iron oxide nanoparticles) at a comparable iron amount; on the other hand, by positron emission tomography (PET), single photon emission computed tomography (SPECT), scintigraphy/x-ray fused imaging, and ex vivo studies it was possible to use FeHA as an imaging agent to detect its dominant accumulation in organs [36]. Additionally, these nanoparticles can be embedded within polymeric networks to devise biomaterials – including scaffolds and coatings on other medically relevant materials, e.g. prosthesis – able to tune the release of functionalized nanoparticles and ions, and intended for the regeneration of different tissues, especially the bone. Nevertheless, when similar particles are used, the potential DNA damage should be considered. This latter ability, i.e. the ability to promote DNA damage, could also be exploited to devise new drug delivery systems for anticancer drugs to promote cell death.

Acknowledgements
Dr. Francesca D'Este is gratefully acknowledged for her skillful assistance in confocal microscopy analyses. Prof. Ivan Donati is gratefully acknowledged for the viscosimetric analyses of chitosan. The skillful assistance of Dr. Massimiliano Dapporto in XRD measurements is gratefully acknowledged. The skillful assistance of Dr. Francesca Carella in ICP-AES is gratefully acknowledged. The skillful assistance of Mr. Michele Magnan in SEM analyses is gratefully acknowledged.

Author contributions
F.F., M.C.M., and G.T. conceived and supervised the study; F.F., M.C.M., and G.T. designed experiments; F.F., M.C.M., A.R., and E.C. performed experiments; F.F. and E.C. analyzed data; F.F. and G.T. wrote the manuscript; F.F., M.C.M., A.R., E.C., M.S., L.F., and G.T. made manuscript revisions.

Funding
This work was made possible through the support of the Departmental Strategic Plan (PSD) of the University of Udine-Interdepartmental Project on Healthy Ageing (2020-25), by additional grants from the University of Udine ('Bando Ricerca Collaborativa' granted by European Community - NextGenerationEU) and from the Consorzio Interuniversitario Biotecnologie - C.I.B. to G.T.

Data availability
The data that support the findings of this study are available from the corresponding author [franco.furlani@uniud.it] upon reasonable request.

Declarations

Ethics approval and consent to participate
Not applicable.

Consent for publication
All authors have seen and approved the submission of the manuscript.

Competing interests
The authors declare no competing interests.

Adherence to national and international regulations
Not applicable.

Received: 2 September 2024 / Accepted: 14 October 2024
Published online: 25 October 2024

References

1. Collins MN, Ren G, Young K, Pina S, Reis RL, Oliveira JM. Scaffold Fabrication Technologies and Structure/Function Properties in Bone Tissue Engineering. Adv Funct Mater [Internet]. 2021;31. https://onlinelibrary.wiley.comhttps://doi.org/10.1002/adfm.202010609
2. Kim C, Lee JW, Heo JH, Park C, Kim DH, Yi GS et al. Natural bone-mimicking nanopore-incorporated hydroxyapatite scaffolds for enhanced bone tissue regeneration. Biomater Res [Internet]. 2022 [cited 2024 Sep 30];26. https://doi.org/10.1186/s40824-022-00253-x
3. Abbasi N, Hamlet S, Love RM, Nguyen NT. Porous scaffolds for bone regeneration. J Science: Adv Mater Devices. 2020;5:1–9.
4. Van Liang hedeD, Anania B, Barzegari S, Verlée M, Nolens B et al. G,. 3D-Printed Synthetic Hydroxyapatite Scaffold With In Silico Optimized Macrostructure Enhances Bone Formation In Vivo. Adv Funct Mater [Internet]. 2022 [cited 2024 Sep 30];32:2105002. https://onlinelibrary.wiley.com/doi/full/https://doi.org/10.1002/adfm.202105002
5. Chen M, Sun Y, Hou Y, Luo Z, Li M, Wei Y, et al. Constructions of ROS-responsive titanium-hydroxyapatite implant for mesenchymal stem cell recruitment in peri-implant space and bone formation in osteoporosis microenvironment. Bioact Mater. 2022;18:56–71.
6. Filip DG, Surdu V-A, Paduraru AV, Andronescu E, Bellucci S, Filip DG et al. Current Development in Biomaterials—Hydroxyapatite and Bioglass for Applications in Biomedical Field: A Review. Journal of Functional Biomaterials 2022, Vol 13, Page 248 [Internet]. 2022 [cited 2024 Sep 30];13:248. https://www.mdpi.com/2079-4983/13/4/248/htm.
7. Zhang Q, Ma L, Ji X, He Y, Cui Y, Liu X et al. High-Strength Hydroxyapatite Scaffolds with Minimal Surface Macrostructures for Load-Bearing Bone Regeneration. Adv Funct Mater [Internet]. 2022 [cited 2024 Sep 30];32:2204182. https://onlinelibrary.wiley.com/doi/full/https://doi.org/10.1002/adfm.202204182
8. George SM, Nayak C, Singh I, Balani K. Multifunctional Hydroxyapatite Composites for Orthopedic Applications: A Review. ACS Biomater Sci Eng [Internet]. 2022 [cited 2024 Sep 30];8:3162–86. https://pubs.acs.org/doi/full/https://doi.org/10.1021/acsbiomaterials.2c00140
9. Ielo I, Calabrese G, De Luca G, Conoci S. Recent Advances in Hydroxyapatite-Based Biocomposites for Bone Tissue Regeneration in Orthopedics. International Journal of Molecular Sciences. 2022, Vol 23, Page 9721 [Internet]. 2022 [cited 2024 Sep 30];23:9721. https://www.mdpi.com/1422-0067/23/17/9721/htm
10. Campodoni E, Dozio SM, Panseri S, Montesi M, Tampieri A, Sandri M. Mimicking natural microenvironments: design of 3D-Aligned Hybrid Scaffold for dentin regeneration. Front Bioeng Biotechnol. 2020.
11. Radulescu DE, Vasile OR, Andronescu E, Ficai A. Latest Research of Doped Hydroxyapatite for Bone Tissue Engineering. Int J Mol Sci. Multidisciplinary Digital Publishing Institute (MDPI); 2023.
12. Sprio S, Dapporto M, Preti L, Mazzoni E, Iaquinta MR, Martini F et al. Enhancement of the Biological and Mechanical performances of Sintered Hydroxyapatite by multiple ions Doping. Front Mater. 2020;7.

13. Jiang X, Zhao Y, Wang C, Sun R, Tang Y. Effects of physico-chemical properties of ions-doped hydroxyapatite on adsorption and release performance of doxorubicin as a model anticancer drug. Mater Chem Phys. 2022;276.
14. Montesi M, Panseri S, Dapporto M, Tampieri A, Sprio S. Sr-substituted bone cements direct mesenchymal stem cells, osteoblasts and osteoclasts fate. PLoS ONE. 2017;12:1–13.
15. Zhong Z, Wu X, Wang Y, Li M, Li Y, Liu XL, et al. Zn/Sr dual ions-collagen co-assembly hydroxyapatite enhances bone regeneration through procedural osteo-immunomodulation and osteogenesis. Bioact Mater. 2022;10:195–206.
16. Tampieri A, D'Alessandro T, Sandri M, Sprio S, Landi E, Bertinetti L, et al. Intrinsic magnetism and hyperthermia in bioactive Fe-doped hydroxyapatite. Acta Biomater. 2012;8:843–51.
17. Iafisco M, Drouet C, Adamiano A, Pascaud P, Montesi M, Panseri S, et al. Superparamagnetic iron-doped nanocrystalline apatite as a delivery system for doxorubicin. J Mater Chem B. 2016;4:57–70.
18. Landi E, Tampieri A, Celotti G, Sprio S. Densification behaviour and mechanisms of synthetic hydroxyapatites. J Eur Ceram Soc. 2000;20:2377–87.
19. Landi E, Logroscino G, Proietti L, Tampieri A, Sandri M, Sprio S. Biomimetic Mg-substituted hydroxyapatite: from synthesis to in vivo behaviour. J Mater Sci Mater Med. 2008;19:239–47.
20. Yang J, Du Y, Yao Y, Liao Y, Wang B, Yu X et al. Employing Piezoelectric Mg2+-Doped Hydroxyapatite to target death receptor-mediated necroptosis: a strategy for amplifying Immune activation. Adv Sci. 2024;11.
21. Furlani F, Pota G, Rossi A, Luciani G, Campodoni E, Mocerino F et al. Designing bioinspired multifunctional nanoplatforms to support wound healing and skin regeneration: Mg-hydroxyapatite meets melanins. Colloids Surf B Biointerfaces. 2024;235.
22. Campodoni E, Montanari M, Artusi C, Bassi G, Furlani F, Montesi M et al. Calcium-based biomineralization: A smart approach for the design of novel multifunctional hybrid materials. Journal of Composites Science. MDPI; 2021.
23. Xue X, Hu Y, Deng Y, Su J. Recent advances in design of functional biocompatible hydrogels for bone tissue Engineering. Adv Funct Mater. John Wiley and Sons Inc; 2021.
24. Islam MM, Shahruzzaman M, Biswas S, Nurus Sakib M, Rashid TU. Chitosan based bioactive materials in tissue engineering applications-A review. Bioact Mater KeAi Commun Co; 2020. pp. 164–83.
25. Rinaudo M. Chitin and chitosan: Properties and applications. Progress in Polymer Science (Oxford) [Internet]. 2006;31:603–32. http://linkinghub.elsevier.com/retrieve/pii/S0079670006000530
26. Furlani F, Marfoglia A, Marsich E, Donati I, Sacco P. Strain Hardening in Highly Acetylated Chitosan Gels. Biomacromolecules. 2021.
27. Sacco P, Furlani F, Marfoglia A, Cok M, Pizzolitto C, Marsich E et al. Temporary/Permanent Dual Cross-link gels formed of a Bioactive Lactose-Modified Chitosan. Macromol Biosci. 2020;2000236.
28. Sacco P, Furlani F, Cok M, Travan A, Borgogna M, Marsich E, et al. Boric Acid Induced transient cross-links in Lactose-Modified Chitosan (Chitlac). Biomacromolecules. 2017;18:4206–13.
29. Furlani F, Sacco P, Decleva E, Menegazzi R, Donati I, Paoletti S et al. Chitosan Acetylation Degree Influences the Physical Properties of Polysaccharide Nanoparticles: Implication for the Innate Immune Cells Response. ACS Appl Mater Interfaces [Internet]. 2019;11:9794 – 9803. http://www.ncbi.nlm.nih.gov/pubmed/307688970A/http://pubs.acs..https://doi.org/10.1021/acsami.8b21791
30. Furlani F, Sacco P, Cok M, De Marzo G, Marsich E, Paoletti S, et al. Biomimetic, Multiresponsive, and Self-Healing Lactose-Modified Chitosan (CTL)-Based gels formed via competitor-assisted mechanism. ACS Biomater Sci Eng. 2019;5:5539–47.
31. Güneş M, Yalçın B, Burgazlı AY, Tagorti G, Yavuz E, Akarsu E et al. Morphologically different hydroxyapatite nanoparticles exert differential genotoxic effects in Drosophila. Sci Total Environ. 2023;904.
32. Jantová S, Theiszová M, Letašiová S, Birošová L, Palou TM. In vitro effects of fluor-hydroxyapatite, fluorapatite and hydroxyapatite on colony formation, DNA damage and mutagenicity. Mutat Res Genet Toxicol Environ Mutagen. 2008;652:139–44.
33. Yamagishi SI, Edelstein D, Du XL, Kaneda Y, Guzmán M, Brownlee M. Leptin induces mitochondrial superoxide production and monocyte chemoattractant Protein-1 expression in aortic endothelial cells by increasing fatty acid oxidation via protein kinase A. J Biol Chem. 2001;276:25096–100.
34. Li H, Junk P, Huwiler A, Burkhardt C, Wallerath T, Pfeilschifter J, et al. Dual effect of ceramide on human endothelial cells: induction of oxidative stress and transcriptional upregulation of endothelial nitric oxide synthase. Circulation. 2002;106:2250–6.
35. Sprio S, Campodoni E, Sandri M, Preti L, Keppler T, Müller FA et al. A graded multifunctional hybrid scaffold with superparamagnetic ability for periodontal regeneration. Int J Mol Sci. 2018;19.
36. Adamiano A, Iafisco M, Sandri M, Basini M, Arosio P, Canu T et al. On the use of superparamagnetic hydroxyapatite nanoparticles as an agent for magnetic and nuclear in vivo imaging. Acta Biomater [Internet]. 2018;73:458–69. https://doi.org/10.1016/j.actbio.2018.04.040
37. Ślósarczyk A, Paszkiewicz Z, Paluszkiewicz C. FTIR and XRD evaluation of carbonated hydroxyapatite powders synthesized by wet methods. J Mol Struct. 2005;744:657–61.
38. Li Z, Yubao LI, Aiping Y, Xuelin P, Xuejiang W. Preparation and in vitro investigation of chitosan/nano-hydroxyapatite composite used as bone substitute materials. J Mater Sci Mater Med. 2005;16:213–9.
39. Chen F, Wang Z-C, Lin C-J. Preparation and characterization of nano-sized hydroxyapatite particles and hydroxyapatite/chitosan nano-composite for use in biomedical materials. Mater Lett [Internet]. 2002;57:858–61. Available from:. www.elsevier.com/locate/matlet.
40. Wang Q, Tang Y, Ke Q, Ke Q, Yin W, Zhang C, et al. Magnetic lanthanum-doped hydroxyapatite/chitosan scaffolds with endogenous stem cell-recruiting and immunomodulatory properties for bone regeneration. J Mater Chem B. 2020;8:5280–92.
41. JCPDS. International Centre for Diffraction Data. 1998.
42. Romanello M, Codognotto A, Bicego M, Pines A, Tell G, D'Andrea P. Autocrine/paracrine stimulation of purinergic receptors in osteoblasts: contribution of vesicular ATP release. Biochem Biophys Res Commun. 2005;331:1429–38.
43. Costessi A, Pines A, D'Andrea P, Romanello M, Damante G, Cesaratto L, et al. Extracellular nucleotides activate Runx2 in the osteoblast-like HOBIT cell line: a possible molecular link between mechanical stress and osteoblasts' response. Bone. 2005;36:418–32.
44. Gibellini D, De Crignis E, Ponti C, Cimatti L, Borderi M, Tschon M, et al. HIV-1 triggers apoptosis in primary osteoblasts and HOBIT cells through TNFα activation. J Med Virol. 2008;80:1507–14.
45. Giuliani N, Girasole G, Vescovi PP, Passeri G, Pedrazzoni M. Ethanol and Acetaldehyde Inhibit the Formation of Early Osteoblast Progenitors in Murine and Human Bone Marrow Cultures. 1999.
46. Keeting,' PE, Scott RE, Colvard DS, Anderson MA, Oursler,' MJ, Spelsberg,' TC, et al. Development and characterization of a rapidly proliferating, well-differentiated cell line derived from normal adult human osteoblast-like cells transfected with SV40 large T Antigen. JOURNAL OF BONE AND MINERAL RESEARCH. Publishers: Mary Ann Liebert, Inc.; 1992.
47. Wei J, Jia J, Wu F, Wei S, Zhou H, Zhang H, et al. Hierarchically microporous/macroporous scaffold of magnesium-calcium phosphate for bone tissue regeneration. Biomaterials. 2010;31:1260–9.
48. Fois MG, Tahmasebi Birgani ZN, Guttenplan APM, van Blitterswijk CA, Giselbrecht S, Habibović P et al. Assessment of cell–material interactions in three dimensions through dispersed coaggregation of Microsized Biomaterials into tissue spheroids. Small. 2022;18.
49. Hélary G, Noirclère F, Mayingi J, Migonney V. A new approach to graft bioactive polymer on titanium implants: improvement of MG 63 cell differentiation onto this coating. Acta Biomater. 2009;5:124–33.
50. Kern S, Eichler H, Stoeve J, Klüter H, Bieback K. Comparative analysis of mesenchymal stem cells from bone marrow, umbilical cord blood, or adipose tissue. Stem Cells. 2006;24:1294–301.
51. Lee MW, Kim DS, Yoo KH, Kim HR, Jang IK, Lee JH, et al. Human bone marrow-derived mesenchymal stem cell gene expression patterns vary with culture conditions. Blood Res. 2013;48:107–14.
52. Furlani F, Rossi A, Grimaudo MA, Bassi G, Giusto E, Molinari F et al. Controlled Liposome Delivery from Chitosan-based Thermosensitive Hydrogel for Regenerative Medicine. Int J Mol Sci. 2022;23.
53. Fernandes Patrício TM, Panseri S, Montesi M, Iafisco M, Sandri M, Tampieri A et al. Superparamagnetic hybrid microspheres affecting osteoblasts behaviour. Mater Sci Eng C. 2019.
54. Yang Y, Yang J, Zhu N, Qiu H, Feng W, Chen Y et al. Tumor-targeting hydroxyapatite nanoparticles for remodeling tumor immune microenvironment (TIME) by activating mitoDNA-pyroptosis pathway in cancer. J Nanobiotechnol. 2023;21.
55. Krishnakumar GS, Gostynska N, Dapporto M, Campodoni E, Montesi M, Panseri S, et al. Evaluation of different crosslinking agents on hybrid biomimetic collagen-hydroxyapatite composites for regenerative medicine. Int J Biol Macromol. 2018;106:739–48.
56. Tampieri A, Iafisco M, Sandri M, Panseri S, Cunha C, Sprio S, et al. Magnetic bioinspired hybrid nanostructured collagen-hydroxyapatite scaffolds

supporting cell proliferation and tuning regenerative process. ACS Appl Mater Interfaces. 2014;6:15697–707.
57. Meng F, Yao D, Shi Y, Kabakoff J, Wu W, Reicher J et al. Oxidation of the cysteine-rich regions of parkin perturbs its E3 ligase activity and contributes to protein aggregation. Mol Neurodegener. 2011;6.
58. Rhee SG. Overview on Peroxiredoxin. Mol Cells. 2016;39:1–5.
59. Perkins A, Nelson KJ, Parsonage D, Poole LB, Karplus PA. Peroxiredoxins: Guardians against oxidative stress and modulators of peroxide signaling. Trends Biochem Sci. Elsevier Ltd; 2015. pp. 435–45.
60. Cesaratto L, Vascotto C, D'Ambrosio C, Scaloni A, Baccarani U, Paron I, et al. Overoxidation of peroxiredoxins as an immediate and sensitive marker of oxidative stress in HepG2 cells and its application to the redox effects induced by ischemia/reperfusion in human liver. Free Radic Res. 2005;39:255–68.
61. Yu J, Zhao F, Gao W, Yang X, Ju Y, Zhao L, et al. Magnetic reactive oxygen species nanoreactor for switchable magnetic resonance imaging guided Cancer Therapy based on pH-Sensitive Fe5C2@Fe3O4 nanoparticles. ACS Nano. 2019;13:10002–14.
62. Jing X, Du T, Chen K, Guo J, Xiang W, Yao X, et al. Icariin protects against iron overload-induced bone loss via suppressing oxidative stress. J Cell Physiol. 2019;234:10123–37.
63. Lin RH, Hung HS, Tang CM, Tsou HK, Chen PH, Yueh CY et al. In vitro biocompatibility of polycaprolactone/hydroxyapatite nanocomposite membranes modified by oleic acid for bone regeneration. Colloids Surf Physicochem Eng Asp. 2024;688.
64. Pu X, Wang Z, Klaunig JE. Alkaline comet assay for assessing DNA damage in individual cells. Curr Protoc Toxicol. 2015;2015:3.12.1–3.12.11.
65. Liu T, Sun L, Zhang Y, Wang Y, Zheng J. Imbalanced GSH/ROS and sequential cell death. J Biochem Mol Toxicol. John Wiley and Sons Inc; 2022.
66. Tang H, Li C, Zhang Y, Zheng H, Cheng Y, Zhu J, et al. Targeted manganese doped silica nano GSH-cleaner for treatment of liver cancer by destroying the intracellular redox homeostasis. Theranostics. 2020;10:9865–87.
67. Mei C, Lei L, Tan LM, Xu XJ, He BM, Luo C, et al. The role of single strand break repair pathways in cellular responses to camptothecin induced DNA damage. Biomedicine and Pharmacotherapy. Elsevier Masson SAS; 2020.
68. Higo T, Naito AT, Sumida T, Shibamoto M, Okada K, Nomura S et al. DNA single-strand break-induced DNA damage response causes heart failure. Nat Commun. 2017;8.
69. Revet I, Feeney L, Bruguera S, Wilson W, Dong TK, Oh DH, et al. Functional relevance of the histone γH2Ax in the response to DNA damaging agents. Proc Natl Acad Sci U S A. 2011;108:8663–7.
70. Podhorecka M, Skladanowski A, Bozko P. H2AX phosphorylation: its role in DNA damage response and cancer therapy. J Nucleic Acids. 2010.
71. Kinner A, Wu W, Staudt C, Iliakis G. Gamma-H2AX in recognition and signaling of DNA double-strand breaks in the context of chromatin. Nucleic Acids Res. 2008. pp. 5678–94.
72. Deng X, Cao M, Zhang J, Hu K, Yin Z, Zhou Z et al. Hyaluronic acid-chitosan nanoparticles for co-delivery of MiR-34a and doxorubicin in therapy against triple negative breast cancer. Biomaterials [Internet]. 2014;35:4333–44. https://doi.org/10.1016/j.biomaterials.2014.02.006
73. Lallana E, De La Rosa R, Tirella JM, Pelliccia A, Gennari M, Stratford A. Chitosan/Hyaluronic Acid nanoparticles: Rational Design Revisited for RNA delivery. Mol Pharm. 2017;14:2422–36.
74. Almalik A, Donno R, Cadman CJ, Cellesi F, Day PJ, Tirelli N. Hyaluronic acid-coated chitosan nanoparticles: Molecular weight-dependent effects on morphology and hyaluronic acid presentation. Journal of Controlled Release [Internet]. 2013;172:1142–50. https://doi.org/10.1016/j.jconrel.2013.09.032
75. Almalik A, Karimi S, Ouasti S, Donno R, Wandrey C, Day PJ et al. Hyaluronic acid (HA) presentation as a tool to modulate and control the receptor-mediated uptake of HA-coated nanoparticles. Biomaterials [Internet]. 2013;34:5369–80. https://doi.org/10.1016/j.biomaterials.2013.03.065
76. Gholap AD, Kapare HS, Pagar S, Kamandar P, Bhowmik D, Vishwakarma N et al. Exploring modified Chitosan-based gene delivery technologies for therapeutic advancements. Int J Biol Macromol. 2024;260.
77. Strand SP, Lelu S, Reitan NK, de Lange Davies C, Artursson P, Vårum KM. Molecular design of chitosan gene delivery systems with an optimized balance between polyplex stability and polyplex unpacking. Biomaterials. 2010;31:975–87.
78. Bravo-Anaya LM, Soltero JFA, Rinaudo M. DNA/chitosan electrostatic complex. Int J Biol Macromol. 2016;88:345–53.
79. Petermann E, Lan L, Zou L. Sources, resolution and physiological relevance of R-loops and RNA–DNA hybrids. Nat Rev Mol Cell Biol Nat Res; 2022. pp. 521–40.
80. Barroso S, Herrera-Moyano E, Muñoz S, García-Rubio M, Gómez-González B, Aguilera A. The DNA damage response acts as a safeguard against harmful DNA–RNA hybrids of different origins. EMBO Rep. 2019;20.
81. Zhang X, He F, Xiang K, Zhang J, Xu M, Long P, et al. CD44-Targeted facile enzymatic activatable Chitosan nanoparticles for efficient antitumor therapy and reversal of Multidrug Resistance. Biomacromolecules. 2018;19:883–95.
82. Wang J, Wu Y, Li H, Kang W, Li W, Fu S. Antitumor effects of polydopamine coated hydroxyapatite nanoparticles and its mechanism: Mitochondria-targeted ROS and calcium channels. Biomaterials Adv. 2024;161.
83. Mushtaq A, Ma X, Farheen J, Lin X, Tayyab M, Iqbal MZ et al. Facile synthesis of metformin loaded Mn3O4-HAp magnetic hydroxyapatite nanocomposites for T1-magnetic resonance imaging guided targeted chemo-phototherapy in vitro. Colloids Surf Physicochem Eng Asp. 2023;674.

Publisher's note